Computers and Geotechnics 154 (2023) 105157

Contents lists available at ScienceDirect

Computers and Geotechnics

journal homepage: www.elsevier.com/locate/compgeo

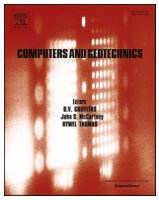

B-SDM: A bounding surface stiffness degradation method for modelling the long-term ratcheting response of offshore wind turbine foundations

Zhiwei Gao [a,*], Luoyi Yan [b], Scott Whyte [c]

[a] James Watt School of Engineering, University of Glasgow, Glasgow G12 8QQ, UK
[b] Department of Civil Engineering, Zhejiang University, Hangzhou 310058, China
[c] Geowynd, 17 Grosvenor Street, London W1K 4QG, UK

ARTICLE INFO

Keywords:
Monopile
Constitutive model
Sand
Cyclic ratcheting
Stiffness degradation

ABSTRACT

Long-term cyclic loading from environmental conditions can lead to excessive permanent rotation of offshore wind turbines (OWTs) due to the ratcheting response of sand. A practical hybrid strain accumulation approach, termed the bounding surface stiffness degradation method (B-SDM), for finite element analysis (FEA)-based design of OWTs under cyclic loading is presented. This method includes a base elastoplastic constitutive model that captures the stress–strain relationship in the first load-unload cycle and a cyclic strain accumulation scheme for modelling the subsequent cycles. The presented approach allows for a versatile overlay scheme that calculates cyclic strain accumulation to be applied to a range of base elastoplastic models. The base constitutive model utilised is established based on the bounding surface concept and considers strain-hardening and plastic volume change before failure. The method has been validated by single element test data on sand and used in finitesingle-element element modelling of monopile response in cyclic loading. When the monopile response is modelled in 3D FEA, the conventional step-by-step modelling approach is used until the end of the first regular cycle. Strain accumulation in subsequent cycles is modelled using the B-SDM, in which the plastic modulus and dilatancy relationship are scaled based on a strain accumulation law.

1. Introduction

Offshore wind power is very important for the world to achieve the net-zero target. Numerous offshore wind farms are already in operation, with many more being constructed and planned around the world. Foundations of offshore wind turbines (OWTs) are a crucial part of the windfarms, and they contribute to a significant percentage of the overall cost. There are different types of foundations for OWT, such as the monopiles, gravity base, jacket and suction caissons (Staubach and Wichtmann, 2020; Page et al., 2021). Monopiles are currently the most widely adopted fixed-foundation option adopted to support OWTs, in water depths typically up to 50 m, due to economic considerations. Monopiles are currently being designed with diameters of up to 12 m and length-to-diameter (L/D) ratios typically between 2.5 and 5. Monopiles are subjected to long-term cyclic lateral loading from the wind and waves, which can cause permanent rotation of the OWT (Andersen, 2009; Andersen, 2015; Staubach and Wichtmann, 2020). The accumulated rotation must be accurately predicted as part of the design to ensure it is within the strict operating limits for OWTs.

Monopiles are now routinely designed based on advanced numerical modelling using 3D finite element analysis (FEA) when monotonic loading is concerned (e.g. Burd et al. 2020; Byrne et al., 2020; Taborda et al., 2020). However, for long-term cyclic ratcheting design checks simplified 0D macro element models (LeBlanc et al., 2010; Abadie et al., 2019) are typically preferred adopting empirical ratcheting functions from model scale pile load tests. Although 0D macro element models are computationally efficient, parameter calibration is typically intrinsically empirical since the cyclic stress–strain element laboratory test data cannot be used for calibration directly unless cyclic 3D FEA is performed to calibrate the 0D model. Therefore, FEA-based OWT design in cyclic loading has also been developed. For FEA-based monopile design in cyclic loading, a proper constitutive model is crucial. Many advanced constitutive models have been proposed for modelling the cyclic behaviour of sand (e.g., Wang et al., 1990; Yang et al., 2003; Ling and Yang, 2006; Wang and Xie, 2014; Corti et al., 2016; Liu et al., 2020; Liao and Yang, 2021; Liao et al., 2022; Yang et al., 2002; Simonin et al., 2003). These models can give good prediction for the single-element test data under various loading conditions. Though some of them have been

* Corresponding author.
E-mail address: Zhiwei.gao@glasgow.ac.uk (Z. Gao).

https://doi.org/10.1016/j.compgeo.2022.105157
Received 16 October 2022; Received in revised form 16 November 2022; Accepted 22 November 2022
Available online 5 December 2022
0266-352X/© 2022 The Author(s). Published by Elsevier Ltd. This is an open access article under the CC BY license (http://creativecommons.org/licenses/by/4.0/).

used in investigating the monopile response in cyclic lateral loading in the literature (e.g., Liu et al., 2021; Liu and Kaynia, 2022), they are rarely used in offshore foundation design. There are two major reasons for this: (a) These models always have complex formulations and some of the key model parameters are hard to determine. The strain-softening of these models can make the solution mesh-dependent and nonlocal regularization is essential (Gao et al., 2022); (b) It is impractical to use these models in step-by-step modelling of offshore foundation response subjected to long-term cyclic loading (e.g., number of cycles over 1000) due to the excessive computation time required (Whyte et al., 2020; Liu et al., 2021; Liu and Kaynia, 2022). Even when computation time is not a concern, the numerical error accumulated during many load cycles is likely to become unacceptable (Niemunis et al., 2005; Pasten et al., 2014). Furthermore, for cyclic design analysis of monopiles, the focus is on the overall accumulated rotation and not the evolution of stress–-strain behaviour and in turn the hysteretic material damping at each soil element.

Therefore, within the literature, several practical long-term cyclic models have been proposed with a focus on their robustness for FEA-based design and calibration to typical laboratory element test datasets. These design-focused models are less capable of predicting the single element cycle-by-cycle stress–strain relationship of soils than the advanced models but have simpler formulations and are more computationally efficient. Two design-focused modelling techniques: (A) Explicit skip-cycle strain accumulation type models (e.g Suiker and de Borst, 2003; Niemunis et al., 2005; Wichtmann, 2005; François et al., 2010; Wichtmann et al., 2010; Pasten et al., 2014; Staubach and Wichtmann, 2020); (B) Cyclic stiffness degradation method (SDM) type models (Achmus et al., 2009).

Fig. 1 shows the difference in load application history for a step-by-step modelling method and the two design-focused techniques. Explicit skip-cycle strain accumulation type model (i.e. approach A) has been used to simulate the cyclic response of different geotechnical problems, such as railway embankments (Suiker and de Borst, 2003), strip footings (Pasten et al., 2014) and offshore monopiles (Staubach and Wichtmann, 2020). In these methods, the soil response in the first one or two cycles is modelled step-by-step using a conventional plasticity model which can realistically capture the initial cyclic response (Fig. 1b). The strain accumulation in the subsequent cycles is then predicted by a calibrated strain accumulation law that is dependent on various factors such as number of cycles N, average stress ratio η_{av} and cyclic stress amplitude q_{amp} at each stress point within the FEA mesh. Definition of η_{av} and q_{amp} can be found in Wichtmann (2005) and will be further discussed in the subsequent sections. An important feature of these methods is that the direction of strain accumulation is determined based on the stress state at each integration point, which may not comply with the boundary conditions of the boundary value problems modelled. This could thus cause divergence in the global equilibrium iteration making robust implementation complex in commercial implicit FEA codes. Achmus et al. (2009) proposed an alternative simplified approach for modelling strain accumulation in cyclic loading, termed the cyclic stiffness degradation method (SDM), i.e. approach B (Fig. 1c). In their model, the soil response is modelled using a Mohr-Coulomb model with pressure-dependent elastic stiffness. After modelling the first cycle step-by-step, a second load cycle is then performed with modified elastic stiffness that is dependent on a strain accumulation law.

Though significant research and publications have focused on modifications to the explicit skip-cycle strain accumulation method (i.e. approach A), there have been few studies proposing improvements to the original SDM (i.e. approach B). The original model proposed by Achmus et al. (2009) was numerically robust, simple to implement and allowed for a reasonable prediction of the cyclic strain accumulation using a simple SDM approach. However, despite the model's strength and suitability for FEA-based design, it suffers from the following main drawbacks: (a) It could not accurately predict the non-linear monotonic stress–strain response, and hence the state variables used for the cyclic

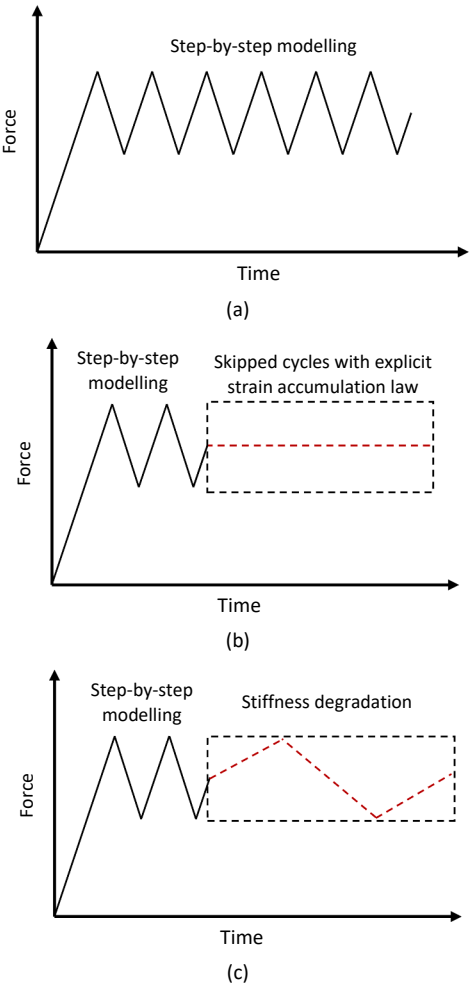

Fig. 1. Illustration of the loading history on monopiles for different modelling methods: (a) sStep-by-step modelling; (b) Skipped-cycle method with a strain accumulation law (method A); (c) Stiffness degradation method (Method B).

accumulation rule, which are typically dependent on the stress state at the end of the first cycle; (b) The initial unload-reload response could not be accurately predicted; (c) The application of multiple packets of different cyclic amplitudes was not considered and (d) the volumetric and deviatoric cyclic strain accumulation could not be individually calibrated and instead was intrinsically fixed to the Poisson's ratio if the soil element does not reach failure.

Therefore, this study presents a modified cyclic SDM approach, termed the B-SDM, for modelling the long-term cyclic ratcheting response of OWTs in sand (Fig. 2). The proposed model and general approach are based on the work by Achmus et al. (2009) but an elastoplastic constitutive model that can properly describe the first regular cycle stress–strain response and is adopted. The soil response in the first regular cycle is modelled using the elastoplastic model via a step-by-step approach. A stiffness degradation phase is then carried out to model the sand response in subsequent cycles with scaled plastic modulus and dilatancy relationship based on a calibrated strain accumulation law. This approach can be easily used for cyclic loading with multiple packets continuously without restarting the simulation at a certain state (Fig. 2b). When the Achmus et al. (2009) method is used, the simulation for the N-th cycle involves two separate simulations. In the first simulation, the state variables for stiffness degradation are obtained. Following this, a second simulation with scaled elastic stiffness is performed starting at the initial configuration without the external load being applied (Fig. 2a). It is thus non-trivial to use this method for

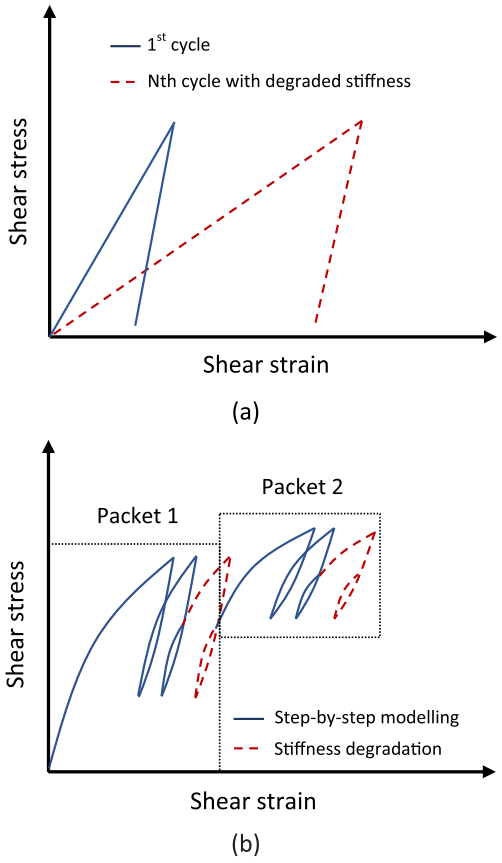

Fig. 2. Comparison between the SDM approaches for modelling cyclic response of a sand element in a constant p triaxial test: (a) Achmus et al. (2009) method with nonlinear elastic Mohr-Coulomb model and (b) the current B-SDM.

modelling multiple packets with different loading conditions.

In the following sections, the constitutive model will first be presented. The constitutive model and cyclic strain accumulation scheme are validated by single element test results on sand in the North Sea. Implementation of the B-SDM for 3D FEA and application in monopile modelling is then presented, highlighting the robustness of the approach for practical cyclic design considering a large number of cycles.

2. Base constitutive model

2.1. The bounding surface model framework

The constitutive model is based on the bounding surface model proposed by Li (2002). Some modifications have been made to the base model for practical applications: (a) The effect of void ratio on sand response is not considered to simplify the model formulations. As a result, different model parameters should be used for sand with various densities, including those for the elastic stiffness, dilatancy and plastic hardening. However, this can be easily adopted for offshore applications, where CPTs are typically performed at all OWT locations and site-specific CPT-parameter correlations are derived from twinned laboratory test data. A further benefit of this parameterisation approach is that the design model parameters are less black box for review, for example, there is a peak friction angle design soil profile as opposed to this being dependent on many different parameters and the soil state (e.g., void ratio and stress level). (b) The strain-softening is not accounted for because most soil elements around the OWTs do not reach strain-softening under either monotonic or cyclic loading. Besides, a constitutive model with strain-softening makes the finite element solution mesh-dependent and in turn, a regularization method has to be introduced which costs excessive computation time for 3D modelling (e.g., Gao et al., 2022).

The stress ratio tensor r_{ij} expressed as below is used in the model formulations

$$r_{ij} = \frac{s_{ij}}{p} = \frac{\sigma_{ij} - p\delta_{ij}}{p} \tag{1}$$

where σ_{ij} is the stress tensor, s_{ij} is the deviatoric stress tensor and δ_{ij} is the Kronecker delta (= 1 for $i = j$ and = 0 for $i \neq j$). The bounding surface $\bar{f}$ is expressed as (Li 2002)

$$\bar{f} = \bar{R}/g(\bar{\theta}) - \bar{H} = 0 \tag{2}$$

where $\bar{R} = \sqrt{3/2\bar{r}_{ij}\bar{r}_{ij}}$ with $\bar{r}_{ij}$ being the 'image' stress ratio tensor of the current stress ratio tensor r_{ij} (Fig. 1), $\bar{H}$ is the size of the bounding surface and $g(\bar{\theta})$ is an interpolation function describing the variation of critical state stress ratio with Lode angle $\bar{\theta}$ (Li 2002)

$$g(\bar{\theta}) = \frac{\sqrt{(1+c^2)^2 + 4c(1-c^2)\sin 3\bar{\theta}} - (1+c^2)}{2(1-c)\sin 3\bar{\theta}} \tag{3}$$

where $c = M_e/M_c$ with M_e and M_c representing the peak stress ratio in triaxial extension and compression. The same mapping rule as discussed in Li (2002) is used in the model (Fig. 3). The projection centre α_{ij} is the same as r_{ij} at the initial state. To avoid numerical issues related to the projection of $\bar{r}_{ij}$ with $r_{ij} = \alpha_{ij}$, $\alpha_{ij} = 0.99r_{ij}$ should be assumed for model implementation at the initial state. Since the focus of this paper is the stiffness degradation method, the bounding surface is briefly introduced. More detailed discussion of the bounding surface and projection law can be found in Li (2002) and Gao and Zhao (2015).

The condition of consistency for the bounding surface, $d\bar{f} = 0$ is expressed as

$$d\bar{f} = p\bar{n}_{ij}d\bar{r}_{ij} - L\bar{K}_p = p\bar{n}_{ij}dr_{ij} - LK_p = 0 \tag{4}$$

where $\bar{n}_{ij} = \frac{\frac{\partial \bar{f}}{\partial \bar{r}_{ij}} - \frac{1}{3}\left(\frac{\partial \bar{f}}{\partial \bar{r}_{mn}}\right)\delta_{mn}\delta_{ij}}{\left\| \frac{\partial \bar{f}}{\partial \bar{r}_{ij}} - \frac{1}{3}\left(\frac{\partial \bar{f}}{\partial \bar{r}_{mn}}\right)\delta_{mn}\delta_{ij} \right\|}$ is the deviatoric unit tensor defined as the norm to $\bar{f}$ at the image stress ratio state $\bar{r}_{ij}$, $\bar{K}_p$ and K_p denote the plastic moduli for the 'image' and current stress state, L is the loading index which is always non-negative. Once L becomes negative, the projection centre must be relocated, which has been discussed in Li (2002). The bounding surface evolves only when the stress state is on the bounding surface and the evolution law is expressed as (Gao and Zhao, 2015)

$$d\bar{H} = L\left\| \frac{\partial \bar{f}}{\partial \bar{r}_{ij}} - \frac{1}{3}\left(\frac{\partial \bar{f}}{\partial \bar{r}_{mn}}\right)\delta_{mn}\delta_{ij} \right\| \frac{\bar{K}_p}{p} \tag{5}$$

The plastic strain increment $d\varepsilon_{ij}^p$ is expressed as

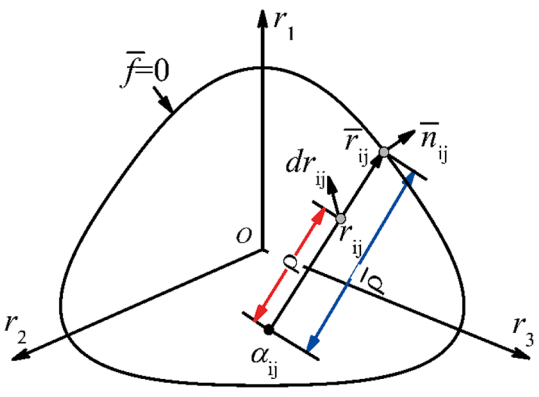

Fig. 3. The bounding surface and mapping rule (Li, 2002).

$$d\varepsilon_{ij}^{p} = de_{ij}^{p} + \frac{1}{3}d\varepsilon_{v}^{p}\delta_{ij} \tag{6}$$

$$de_{ij}^{p} = L\bar{n}_{ij} \tag{7}$$

$$d\varepsilon_{v}^{p} = D\sqrt{\frac{2}{3}de_{ij}^{p}de_{ij}^{p}} = \sqrt{\frac{2}{3}}LD \tag{8}$$

where $d\varepsilon_{v}^{p}$ is the plastic volumetric strain increment, de_{ij}^{p} is the plastic deviatoric strain increment and D is the dilatancy relationship.

2.2. Dilatancy relationship and plastic modulus

The dilatancy relationship is expressed as below (Li and Dafalias, 2000; Li, 2002; Gao et al., 2014)

$$D = d_1\left[M_d g(\bar{\theta})\left(\frac{\bar{\rho}}{\rho}\right) - \bar{R}\right] \tag{9}$$

where d_1 is a model parameter, M_d is the phase transformation stress ratio that is assumed a constant for the soil. The definition of $\bar{\rho}$ and ρ is shown in Fig. 3. When the stress state is inside the bounding surface, $\bar{\rho}/\rho > 1$ and $M_d g(\bar{\theta})\left(\frac{\bar{\rho}}{\rho}\right)$ is typically much bigger than $\bar{R}$, and thus, Eq. (9) gives a predominantly contractive response, which is consistent with the experimental observations (Li, 2002; Wichtmann, 2005). The plastic modulus is

$$K_p = \frac{Gh}{R_d}\left[M_c g(\bar{\theta})\left(\frac{\bar{\rho}}{\rho}\right)^2 - \bar{R}\right] \tag{10a}$$

$$R_d = \sqrt{\frac{3}{2}(r_{ij} - \alpha_{ij})(r_{ij} - \alpha_{ij})} \tag{10b}$$

where G is the elastic shear modulus, h is a factor for the plastic modulus that is dependent on the loading history (Li, 2002)

$$h = h_m\left(\frac{\rho}{\bar{\rho}}\right)^{20} + \left[1 - \left(\frac{\rho}{\bar{\rho}}\right)^{20}\right]h_m h_c \tag{11}$$

Eq. (11) renders $h \approx h_m$ when $\frac{\rho}{\bar{\rho}} = 1$ (virgin loading) and $h \approx h_m h_c$ when $\frac{\rho}{\bar{\rho}} < 1$ (current stress state within the bounding surface). Since sand has higher stiffness when the stress state is within the bounding surface, the parameter h_c is typically greater than 1. At the onset of projection centre relocation, $\frac{\bar{\rho}}{\rho} = \infty$ because $r_{ij} = \alpha_{ij}$, which brings numerical singularities in K_p and D as they both become infinite. To overcome this difficulty, an elastic step is performed when relocation occurs. The plastic modulus for the bounding surface can be obtained by setting $\frac{\rho}{\bar{\rho}} = 1$ in Eq. (9)

$$\bar{K}_p = \frac{Gh_m}{R_a}[M_c g(\theta) - \bar{R}] \tag{12}$$

It should be emphasized that Eq. (11) is only suitable for modelling the drained sand response in the first cycle. But this is sufficient for the present study because the sand response after the first cycle will be modelled using the skipped-cycle approach which will be discussed in the subsequent section.

2.3. Elastic shear and bulk moduli

A pressure-dependent elastic shear modulus expressed below is used

$$G = G_0 p_a\sqrt{p/p_a} \tag{13}$$

where G_0 is a model parameter. The elastic bulk modulus K is a function of G and Poisson's ratio ν

$$K = G\frac{2(1+\nu)}{3(1-2\nu)} \tag{14}$$

Derivation of the constitutive equations can be found in the Appendix. In the following sections, the stress–strain relationship in drained triaxial compression will be presented, which will include the cases for both step-by-step and B-SDM modelling.

3. The bounding surface stiffness degradation model (B-SDM)

The stiffness degradation method will be presented in this section. Focus will be placed on the stress–strain relationship in triaxial compression to facilitate the discussion.

3.1. Single cycle step-by-step stage

The total strain increment for conventional single cycle step-by-step modelling in triaxial compression can be expressed as

$$d\varepsilon_q = d\varepsilon_q^e + d\varepsilon_q^p = \frac{dq}{3G} + \sqrt{\frac{2}{3}}\frac{p\bar{n}_{ij}dr_{ij}}{K_p} \tag{15a}$$

$$d\varepsilon_v = d\varepsilon_v^e + d\varepsilon_v^p = \frac{dp}{K} + \sqrt{\frac{2}{3}}\frac{p\bar{n}_{ij}dr_{ij}}{K_p}D \tag{15b}$$

where ε_q is the shear strain and ε_v is the volumetric strain. The superscripts e and p denote elastic and plastic, respectively. Modelling the cyclic response of sand with multiple cycles using a step-by-step approach is challenging because a complex constitutive model is always needed (e.g., Wang et al., 1990; Yang et al., 2003; Ling and Yang, 2006; Wang and Xie, 2014; Liu et al., 2020). Indeed, the model presented above is only suitable for modelling the soil response in the first cycle. The plastic modulus and dilatancy relationship have to be modified for modelling multiple cycles, which requires more parameters that are difficult to determine (Li, 2002; Gao and Zhao, 2015). Therefore, the B-SDM approach will be used in this study for modelling the monopile response under long-term cyclic loading. Specifically, the first cycle will be modelled step-by-step using the constitutive model (Eq. 15), the plastic modulus and dilatancy will be scaled in a cyclic strain accumulation phase to capture the strain accumulation at the end of N ($N \geq 2$) cycles. This approach is similar to the one proposed by Achmus et al. (2009) but is more suitable for modelling the sand response in monotonic loading and cyclic loading with multiple packets, which has been discussed above.

3.2. Stiffness degradation phase

The B-SDM is illustrated in Fig. 4 for a drained triaxial compression test, in which σ_a is the axial stress, σ_r is the lateral stress that is kept constant at 95 kPa, ε_a is the axial strain, ε_r is the lateral strain and D_r is the relative density. The results in Fig. 4 and other figures below are for fine medium sand in the Dutch Sector, North Sea. There are two steps for the B-SDM modelling of a single-element test in cyclic loading:

Step 1 (A → B): Step-by-step modelling of the soil response in the first cycle. The constitutive model with the original parameters is used to predict the soil response (Eq. 15). The accumulated strain obtained at the end of this cycle is ε_{ij}^{1} (Point B).

Step 2 (B → C): B-SDM step for predicting the strain accumulation ε_{ij}^{N} at the end of N-th cycle. The same loading condition as Step 1 is repeated but the constitutive equation used in the skipped-cycle is expressed as

$$d\varepsilon_q = \frac{dq}{3G} + r_h\sqrt{\frac{2}{3}}\frac{p\bar{n}_{ij}dr_{ij}}{K_p} \tag{16a}$$

$$d\varepsilon_v = \frac{dp}{K} + r_h r_d\sqrt{\frac{2}{3}}\frac{p\bar{n}_{ij}dr_{ij}}{K_p}D \tag{16b}$$

where r_h is a variable dependent on η_{av} and number of cycles N ($N \geq 2$) and r_d is a constant model parameter. The expression of r_h is proposed as below based on the test data from the Dutch Sector, North

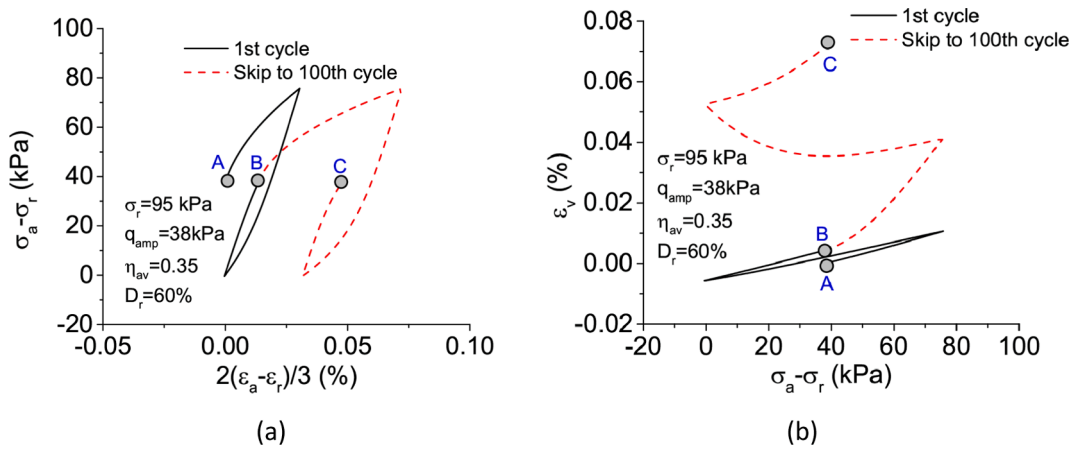

Fig. 4. Illustration of the skipped cycle modelling for strain accumulation at the end of the 100th cycle in a drained cyclic triaxial test: (a) shear strain and shear stress relationship; (b) shear stress and volumetric strain relationship.

Sea and some existing studies (e.g., Suiker and de Borst, 2003; Wichtmann, 2005; Pasten et al., 2014)

$$r_h = \ln[1 + a(N-1)] + b(N-1) \tag{17a}$$

$$b = b_1 \left(\frac{\eta_{av}}{M_c}\right)^{b_2} \tag{17b}$$

where a, b_1 and b_2 are three model parameters. Two model parameters are scaled with other equations unchanged in implementing Eq. (16), including h_m to h_m/r_h for the plastic modulus and d_1 to $d_1 r_d$ for the dilatancy relationship.

The bounding surface size $\overline{H}$ and projection centre α_{ij} are reset at the beginning of Step 2 to make the initial bounding surface conditions for the single cycle step-by-step and cyclic degradation modelling the same. Specifically, $\overline{H}$ is adjusted such that the stress state lies on the bounding surface ($\overline{\rho} = \rho$) and α_{ij} is set at r_{ij}. The soil response would be too stiff due to the bounding surface expansion if this adjustment is not done. The strain accumulation in the stiffness degradation phase is ε_{ij}^{sN} and the total strain accumulation at the end of the N-th cycle is $\varepsilon_{ij}^{N} = \varepsilon_{ij}^{1} + \varepsilon_{ij}^{sN}$. It should be emphasized that the strain accumulation at the end of this step (Point C) represents real soil response while the stress–strain curve (dash line) in Fig. 4 does not, as per the philosophy of the general SDM methodology.

In cyclic loading with a fixed stress amplitude, the elastic strain is fully recovered in one cycle and the accumulated strain is the plastic part. Therefore, the following relationship can be obtained based on Eqs. (15) and (16)

$$\frac{\varepsilon_q^{sN}}{\varepsilon_q^1} = \frac{\varepsilon_q^N - \varepsilon_q^1}{\varepsilon_q^1} = r_h \tag{18a}$$

$$\frac{\varepsilon_v^{sN}}{\varepsilon_v^1} = \frac{\varepsilon_v^N - \varepsilon_v^1}{\varepsilon_v^1} = r_h r_d \tag{18b}$$

Eq. (18) will be used for determining the strain accumulation parameters in Eq. (17).

3.3. Parameter determination and model validation

There are eight parameters for the model, seven of which can be determined based on the monotonic loading test results. All the model parameters are listed in Table 1. Fig. 5 shows the model prediction of a sand, from the North Sea Dutch Sector, with relative density $D_r = 60\%$ in drained triaxial compression. The parameter M_c is the stress ratio at failure in triaxial compression that can be directly obtained from a drained triaxial compression test. c should be determined based on the failure stress ratio in triaxial extension. Since there is no data in triaxial extension, $c = 0.75$ is assumed for this sand. M_d is the phase transformation stress ratio in triaxial compression that can be readily obtained based on the dilatancy of sand in triaxial compression. The elastic stiffness parameter G_0 is determined as the maximum shear stiffness at very low shear strain levels. As the Poisson's ratio ν has small influence on the sand response under drained loading conditions, it is assumed to be 0.2 in this study. The hardening parameter h_m is determined by best fitting the $\varepsilon_1 - q$ relationship in drained triaxial compression (Fig. 3a). Finally, the dilatancy parameter for dilatancy d_1 should be determined by best fitting the $\varepsilon_1 - \varepsilon_v$ relationship (Fig. 5b). Fig. 5b indicates that the model gives unlimited volumetric expansion after phase transformation, which is not realistic when the shear strain is very large. Therefore, a cut-off is implemented for the total volumetric expansion. It is worth mentioning that the parameters can also be determined via optimization or machine learning (Yin et al., 2017; Yin et al., 2018).

Table 1
Parameters for the constitutive model.

Failure	Elasticity	Dilatancy	Hardening
$M_c = 1.39$	$G_0 = 1000$	$d_1 = 0.27$	$h_m = 0.18$
$c = 0.75$	$\nu = 0.2$	$M_d = 0.9$	$h_c = 2$

There is only one parameter for unload-reload which can be determined based on the stress–strain relationship in the first cycle. For the sand used in this study, h_c is determined by best fitting the accumulated shear and volumetric strain at the end of the first cycle. More strain accumulation is predicted as h_c decreases. Fig. 6 shows the model prediction of drained triaxial compression test with different η_{av} and the same q_{amp}. Good agreement between the test data and model prediction can be observed.

Eq. (18) indicates that the parameters a, b_1, b_2 and r_d can be determined using the strain accumulation data in cyclic loading. In this study, a, b_1 and b_2 are determined based on the shear strain accumulation in drained cyclic tests with different η_{av} (Fig. 7). After the parameters for r_h are determined, r_d can be determined to best fit the volumetric strain accumulation (Fig. 8). Table 2 shows all the parameters for strain accumulation. It is evident that the predicted volumetric strain for tests with $\eta_{av} = 0.24$ is higher than the measured data. This can be seen in the dilatancy predicted by the model in the stiffness degradation phase, which indicates clear over prediction of volumetric strain accumulation at $\eta_{av} = 0.24$ at different number of cycles (Fig. 9). In previous studies, it is suggested that the dilatancy relationship of the Modified Cam-Clay (MCC) model can be used for the skipped cycles or stiffness degradation phase (Wichtmann, 2005; Pasten et al., 2014). The results in Fig. 9 shows that the MCC dilatancy relationship gives slightly better

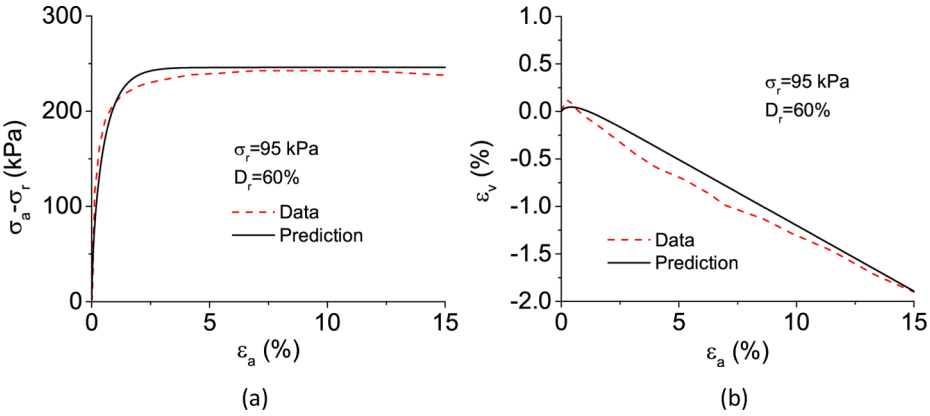

Fig. 5. Model prediction for sand response in drained triaxial compression: (a) $\varepsilon_a - q$ relationship; (b) $\varepsilon_a - \varepsilon_v$ relationship.

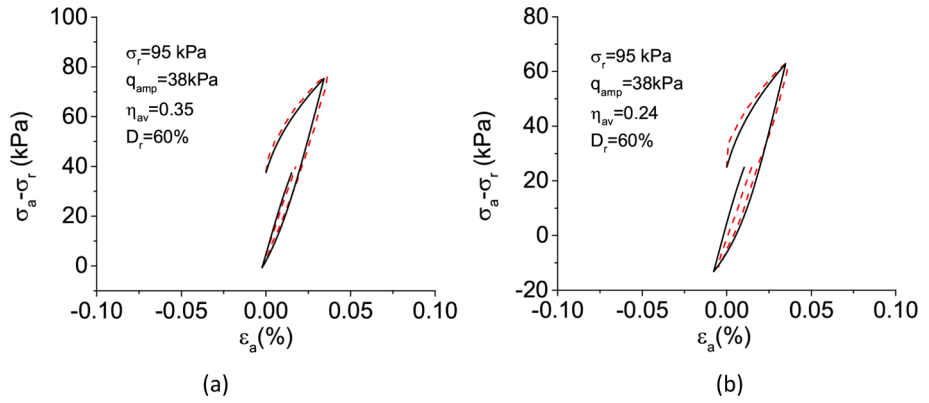

Fig. 6. Model prediction for sand response in drained cyclic triaxial compression (1st cycle): (b) $\eta_{av} = 0.35$; (a)$\eta_{av} = 0.24$.

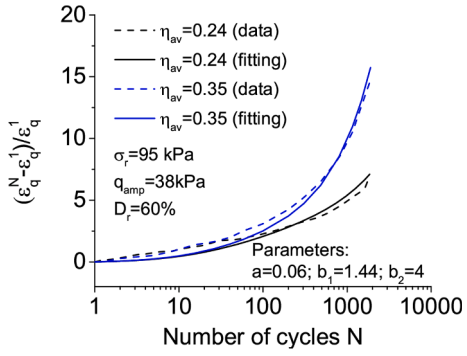

Fig. 7. Determination of the shear strain accumulation parameters based on drained triaxial compression test results.

prediction but still not satisfactory at $\eta_{av} = 0.24$. It is worth noting that the model by Achmus et al. (2009) gives the least satisfactory prediction for dilatancy, because it is only a function of the Poisson's ratio. Therefore, better prediction can be obtained by: (a) using r_d that is dependent on η_{av} and N or (b) a new dilatancy relationship for the stiffness degradation phase. However, this is not explored in this study since there was not extensive cyclic test data available to confirm this hypothesis. Finally, since b has significant influence on r_d and it changes with η_{av} following a power law (Eq. (17b)), it is important to control the upper limit of b for modelling real boundary value problems to avoid very large r_d and excessively large shear strain accumulation being predicted. In this study, the upper limit of b is set at 0.02 due to the lack of test data. A more accurate upper limit of b can be obtained for a more cyclic test dataset within which larger η_{av} and q_{amp} are considered.

4. Implementation of the B-SDM for modelling the monopile behaviour

The constitutive model has been implemented in Plaxis 3D using the explicit stress integration method with error control (Sloan et al., 2001). The tolerance for stress integration error is set at 10^{-4}. A smaller tolerance is found to have little influence on the results but much more computation time is required. There are three major phases for modelling the cyclic response of monopiles using the proposed method, including the step-by-step modelling until the end of the first regular cycle, state variable resetting and skipped-cycle modelling (Fig. 10). These phases are similar to those for the single element modelling. Two consecutive load packets are shown in Fig. 10. In this figure, H_p, H_a and H_m denote the maximum, average and minimum lateral force for the loading packet. The same modelling procedure as described below should be repeated for the other packets:

Phase 1 (O → B or E → G): Step-by-step modelling until the end of the first regular cycle using the sand model with original parameters. At the end of the first regular cycle (B or G), the average stress ratio η_{av} is calculated for each integration point and saved as a state variable for Eq. (17) that will be used in the cyclic strain accumulation modelling in Phase 3.

Phase 2 (B → C or G → H): Resetting the state variables for the cyclic strain accumulation modelling in Phase 3. This is similar to the state variable resetting for Step 2 of the single-element simulation described above. The external load remains the same as that of B or G in this phase. The bounding surface size $\overline{H}$ is adjusted to make $\overline{\rho} = \rho$ and the projection centre is relocated at $\alpha_{ij} = r_{ij}$. When a more complex model of sand is used, other state variables such as the void ratio should also be reset.

Phase 3 (C → D or H → I): Cyclic strain accumulation modelling

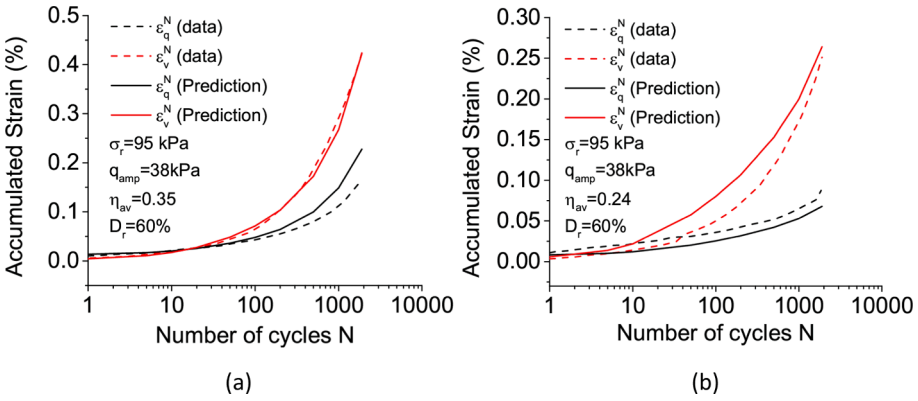

Fig. 8. Model prediction of the strain accumulation on in drained cyclic triaxial compression tests: (a) $\eta_{av} = 0.35$; (b)$\eta_{av} = 0.24$.

Table 2
Strain accumulation model parameters.

Shear strain accumulation	Volumetric strain accumulation
$a = 0.06$	$r_d = 6.2$
$b_1 = 1.44$	
$b_2 = 4$	

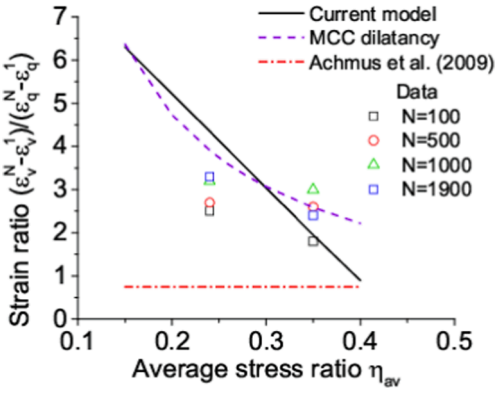

Fig. 9. Comparison between the measured and predicted strain ratio in the stiffness degradation phase.

adopting the B-SDM from the end of the single cycle phase. The variable r_h is calculated based on η_{av} and N using Eq. (17). Two model parameters, h_m and d_1, are then scaled following the rule in Step 2 of single element modelling discussed above. The same loading condition in Phase 1 is repeated. The pile displacement at the end of the N-th cycle can be obtained at the end of this phase.

An intermediate phase is used to reset the state variables at the end of each packet by keeping the external load constant (**D → E or I → J**) and resetting the bounding surface and projection centre. This is the same as Phase 2 above. Note that the loading history at all stress integration points is 'erased' in this resetting phase due to bounding surface adjustment. At the end of Phase 3 (D or I), the bounding surface has expanded for most stress integration points due to loading and unloading in Phase 3, which increases the soil stiffness. Resetting the bounding surface means that such stiffness increase is neglected, which leads to more pile deformation in the next load packet with higher H_p. Although this approach is potentially slightly conservative it is considered robust for design calculations. If an optimised whole-life design type approach was to be adopted (i.e. Gourvenec, 2022) at the start of stage the reloading stages the bounding surface could be updated.

5. Finite element modelling of rigid monopile response under cyclic loading

The monopile modelled is shown in Fig. 11. The pile diameter is 8.8 m and the pile length below the seabed is 25 m. The application point of the lateral force is 35 m above the seabed (denoted as L_h in Fig. 11). Only part of the pile above the seabed (1.5 m) is modelled for simplicity (Fig. 11). The vertical force caused by the weight of the turbine and pile is neglected because it causes negligible deformation in the soil. Therefore, the vertical forces V_1 and V_2 are simply calculated based on the total moment M generated at the centre of the pile by the lateral

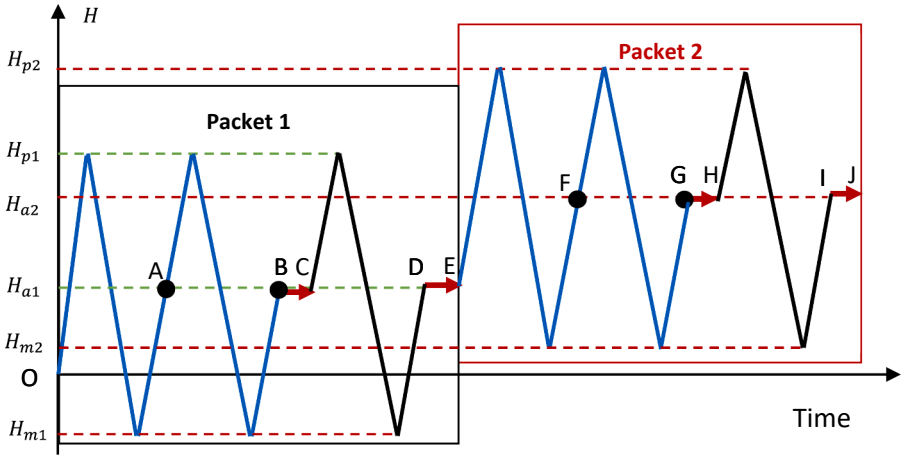

Fig. 10. Loading history for monopile modelling using the B-SDM model.

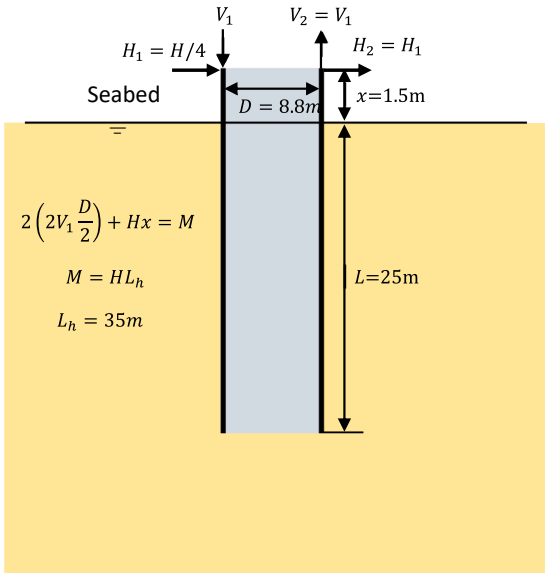

Fig. 11. Dimension and loading condition of the monopile.

force H (see equations in Fig. 11). The saturated unit weight of the soil is $\gamma_s = 20\text{kN/m}^3$. The water level is 26 m above the seabed and $\gamma_w = 10\text{kN/m}^3$. Drained condition is considered. The initial stress state is generated using the K_0 method with isotropic conditions assumed i.e. $K_0 = 1.0$. Effect of K_0 on the pile response will be discussed below. Interface between the soil and outer surface of the pile is modelled. The interface strength is modelled with interface friction angle $\varphi_i = 28^\circ$, cohesion $c_i = 1\text{kPa}$ and dilation angle $\psi_i = 0^\circ$. Stress-dependent interface stiffness is used with $E^i_{oed} = E_{int}\sqrt{\sigma_n/p_a}$, where σ_n is the normal contact stress, E^i_{oed} is the oedometer contact modulus and E_{int} (100 MPa) is the reference value of E^i_{oed} at $\sigma_n = p_a$. The mesh size and coordination system used in the modelling is shown in Fig. 12. A total of 31,660 ten-noded tetrahedron elements are used, based on the parametric study on mesh size effect below. The bottom of the soil is fully fixed while the top surface is free. The displacement in the x and y direction is fixed for the vertical sides perpendicular to the x and y direction, respectively. In all the simulations here, the effect of pile driving process is neglected.

5.1. Monopile lateral response in monotonic loading

Fig. 13a shows the monopile response under monotonic loading with different maximum lateral force H_{max} with the parameters, mesh size and boundary conditions discussed above. Parametric studies on the effect of mesh size, contact stiffness and lateral earth pressure coefficient are presented in Fig. 13b-c. The mesh size is found to have small influence on the relationship between lateral force and pile head rotation θ once the total element number is above 14,000 (Fig. 13b). The contact stiffness is hard to measure and E^i_{oed} is assumed to be similar to G of the soil. Fig. 13b indicates that when E^i_{oed} reduced by 50%, there is less than 10% increase in the pile head rotation at the same lateral load. It should be noted, although shown not to be critical at the displacement levels important for this study, the interface stiffness will influence on the results at very small displacement levels, and therefore, should be considered carefully for natural frequency analysis or fatigue limit state design. The lateral earth pressure coefficient K_0 is also not easy to obtain in either the laboratory or the field and therefore its potential effect on the load-unload response of the monopile was investigated across the range of expected values. Fig. 13d shows that as K_0 decreases by about 50% (i.e.$K_0 = 0.5$), there is about 10% increase in pile head rotation at $H = 23\text{MN}$. Using lower K_0 will thus make the design more conservative when $K_0 < 1$.

5.2. Cyclic pile response in one packet

The model simulation for a single packet of storm load is shown in Fig. 14. During regular cyclic loading, the average lateral force is $H_a = 0.4H_p$ and $H_m = -0.2H_p$, with $H_p = 10\text{MN}$. It is important to point out that the $\theta - H$ relation before the end of the first regular cycle (solid curve in Fig. 14) represents the real pile response while that for the cyclic strain accumulation stage does not (dashed curves). Only the accumulated θ at the end of skipped cycles represent real pile behaviour (Points A and B in Fig. 14). This is similar to the single element simulations shown in Fig. 4, where the stress–strain curves in the cyclic strain accumulation stage does not represent real soil response while the strain accumulation at the end of the B-SDM stage does. The $N - \theta$ curve shown in Fig. 15 has a similar shape as that in Fig. 8 that shows the cyclic strain accumulation for a single soil element.

Fig. 16 shows the total displacement contour in the soil at the end of the 10th, 100th, 500th, and 1000th cycles. There is obvious deformation localization near the ground surface, which is consistent with the experimental observations (Lai et al., 2020). Fig. 17 shows the lateral displacement profile of the pile at the end of different numbers of cycle. The pile remains a straight because it is modelled as a rigid body. The point of rotation (zero lateral displacement point) moves up slightly as the cycle number increases but remain at about 20 m below the seabed (80% of the pile length below seabed). This is similar to the centrifuge test results in Lai et al. (2020) and numerical results reported in Achmus et al. (2009). When the pile head rotation is much larger (e.g., >0.5°),

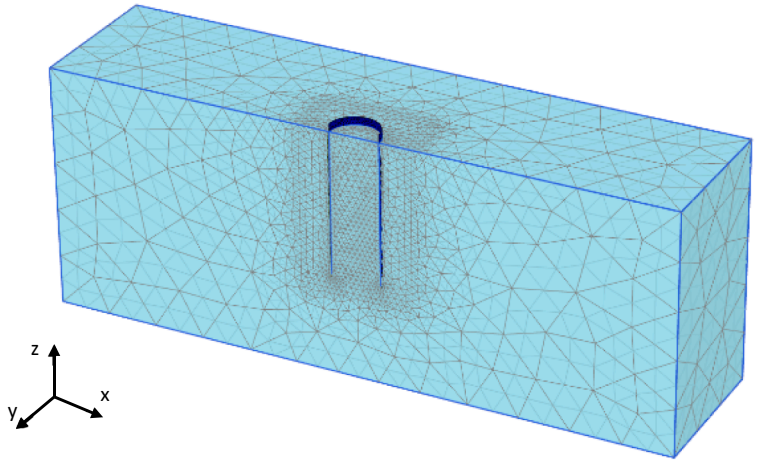

Fig. 12. Finite element mesh for the monopile modelling (31660 elements).

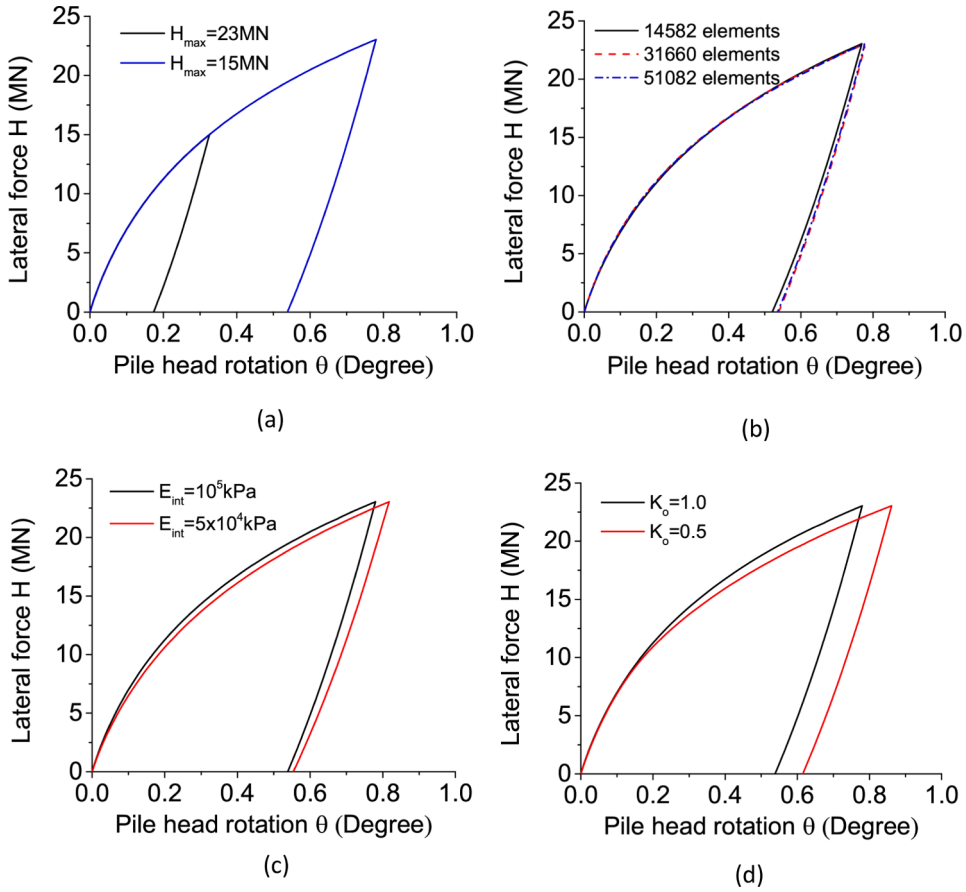

Fig. 13. The relationship between pile head rotation and lateral force in loading and unloading: (a) Effect of H_{max}; (b) Effect of mesh size; (c) Effect of contact stiffness; (d) Effect of.K_0

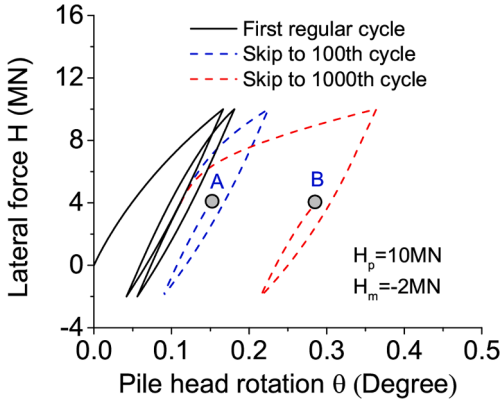

Fig. 14. Pile head rotation determination in a single load packet with different number of cycles.

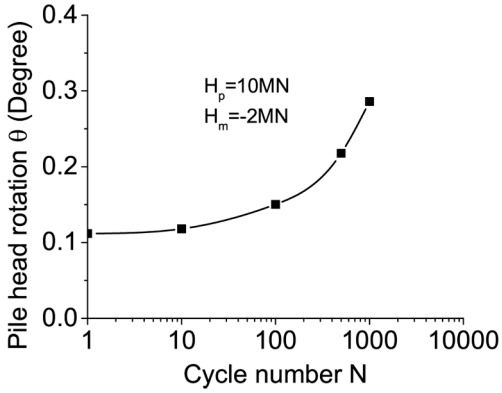

Fig. 15. The relationship number of cycles and pile head rotation in a single packet of storm load.

the point of rotation can move up to a higher position.

The cyclic strain accumulation method here is based on the one proposed by Achmus et al. (2009), in which the soil dilatancy in the stiffness degradation phase is controlled by the Poisson's ratio only before failure. In the current model, the dilatancy during the stiffness degradation phase is affected by both the dilatancy model parameters (Table 1) and strain accumulation parameters (Table 2). Since the dilatancy parameters in Table 1 are determined using monotonic loading test results, r_d is the main parameter that controls the dilatancy in the stiffness degradation phase. Fig. 18 shows the effect of r_d on pile rotation in cyclic loading. More volumetric strain is predicted at higher r_d (Fig. 19). Note that negative volumetric strain in Fig. 19 indicates volumetric contraction due to the sign conversion used by Plaxis. The effect of r_d on pile head rotation is more significant at larger number of cycles (Fig. 18). This indicates that the cyclic accumulation flow rule should be properly considered, especially for the long-term cyclic loading. An important feature of the B-SDM approach is that the cyclic volumetric and shear strain can be calibrated and modelled in a decoupled manner, which from Fig. 18 can be shown to be very important. Using the original SDM elastic coupling of volumetric and shear strains could result in an incorrect prediction of the pile head rotation as shown on Fig. 18.

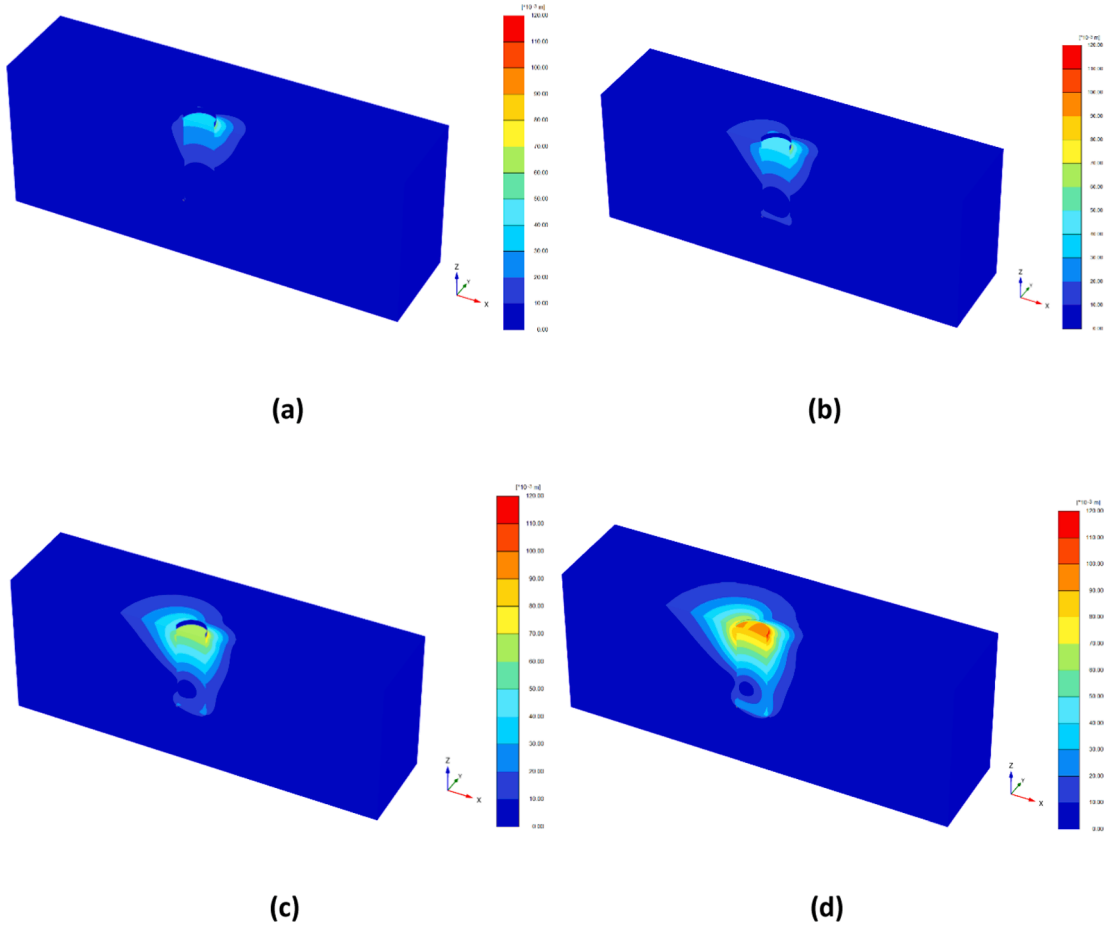

Fig. 16. Total displacement contour of the soil at the end of the (a) 10th cycle, (b) 100th cycle, (c) 500th cycle and (d) 1000th cycle.

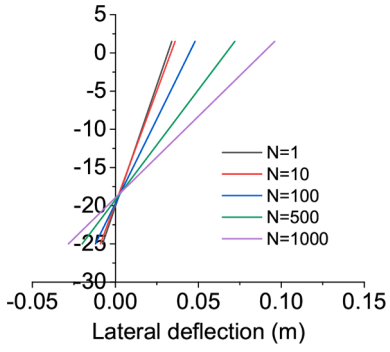

Fig. 17. Lateral displacement profile of the pile at the end of different numbers of cycle.

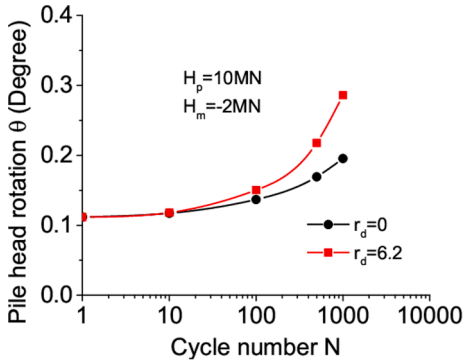

Fig. 18. The effect of r_d on pile head rotation accumulation.

5.3. Cyclic pile response in multiple packets

A cyclic load configuration with multiple packets has also been simulated. The storm loading history is shown in Table 3. The peak horizontal load is $H_{max} = 15$MN. The average and minimum lateral load is $H_a = 0.4H_p$ and $H_a = -0.2H_p$ for each packet, respectively. Two loading conditions, one with ascending H_p and the other with descending H_p. The packet numbers N_p in the brackets are for the case with descending H_p. The relationship between θ and number of packets is shown in Fig. 20. For the case with ascending H_p, pile head rotation increases with N_p and is mainly affected by load packets with higher H_p, although the number of cycles is lower. There is very little rotation accumulation in the first two packets. In the case with decreasing H_p, pile head rotation accumulation mainly occurs in the first packet with the maximum H_p. There is further small rotation accumulation from Packet 2 to Packet 5. There is decrease in the rotation from Packet 6 to Packet 8. This is called self-healing by Staubach and Wichtmann (2020), which occurs as H_p decreases with the number of packets. Such response has also been observed in experiments (Zachert et al., 2015). The reason is that there is significant recovery of pile deformation due to unloading from a packet with high H_p to one with low H_p. During the cyclic loading with low H_p, there will be further deformation accumulation, but this is smaller than the elastic recovery before. Therefore, load packets with ascending H_p should be used for practical design to guarantee safety when this method is used.

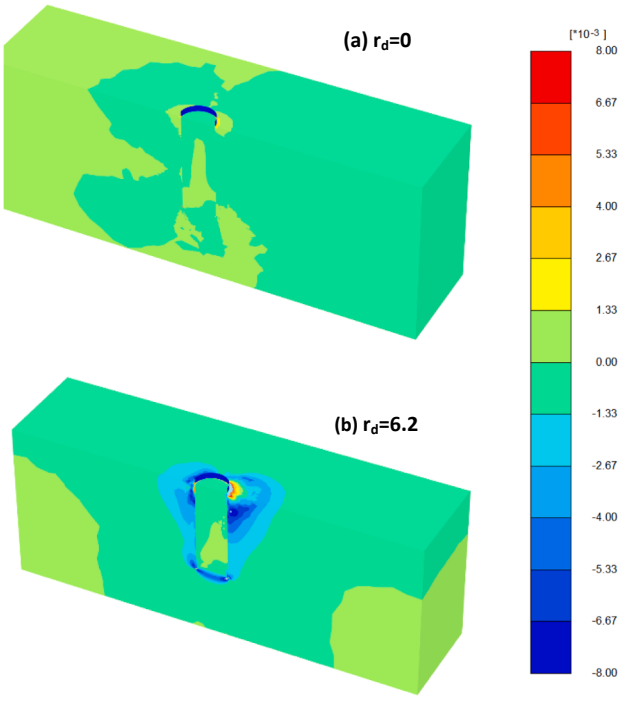

Fig. 19. Effect of parameter r_d on volumetric strain accumulation in the soil: (a) $r_d = 0$ at the end of 1000th cycle; (b) $r_d = 6.2$ at the end of 1000th cycle.

Table 3
Storm loading history (H_{max} = 15MN).

Packet number N_p	H_p/H_{max}	Number of cycles
1(8)	0.05	900
2(7)	0.17	400
3(6)	0.35	320
4(5)	0.55	80
5(4)	0.66	12
6(3)	0.77	6
7(2)	0.9	3
8(1)	1	1

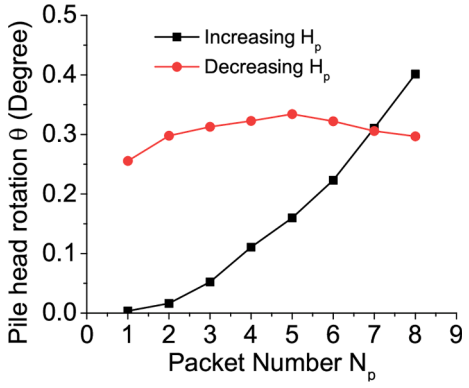

Fig. 20. Pile head rotation in a storm load with multiple packets.

6. Conclusion

A simple and practical cyclic strain accumulation method, termed the B-SDM approach, for modelling the drained ratcheting cyclic response of offshore monopiles in sand is presented. This method has the following features:

(a) A practical bounding surface model that can predict the sand response in the first regular cycle is presented which is suitable for design analysis. The state dependency and strain-softening behaviour of sand is neglected to facilitate practical applications. However, different model parameters should be used for the same sand with different densities using a CPT-parameter calibration approach.
(b) The monopile response before the end of the first regular cycle is modelled using the conventional step-by-step approach. The strain accumulation in the soil and pile displacement in the subsequent cycles are modelled using a cyclic stiffness degradation approach, termed the B-SDM after the work by Achmus et al. (2009), in which the same loading condition of first regular cycle is repeated while scaled plastic modulus and dilatancy relationship are used. The predicted stress–strain relationship during skipped cycles does not represent real soil behaviour but the strain accumulation at the end does.

Though a simple bounding surface model is used here, other proper sand models can also be used for the B-SDM approach. The base constitutive model and B-SDM have been validated by drained cyclic triaxial tests on a sand in the North Sea. The cyclic response of monopiles in cyclic loading has been analysed using finite element modelling. Cyclic loading with multiple packets can be conveniently modelled without restarting the simulations. Main features of pile and soil displacement can be captured. This represents the first step of the B-SDM method development. The model is simple to implement and highly stable for numerical analysis, so is considered ideal for monopile design calculations and is considered superior to the current industry standard approach for long-term cyclic loading which typically considers a macro element model with an empirical calibration. This model could be used directly for design or to provide a site-specific calibration of a macro element model. Further work is required to improve the model in the following key areas:

(a) The strain accumulation formulations need to be further verified and potentially updated, which include both the shear strain accumulation and dilatancy equations. Both equations used here are based on limited test data, which means that it may not work for more general cyclic loading conditions with various stress amplitudes and average stress ratio. In particular, a new dilatancy equation for the stiffness degradation phase can be proposed to better model the volumetric strain accumulation.
(b) The method needs to be validated by either centrifuge or field test on monopiles under cyclic loading (Truong et al., 2019; Lai et al., 2020; Duque et al., 2021), from which corresponding cyclic laboratory data is available for calibration of the B-SDM.

CRediT authorship contribution statement

Zhiwei Gao: Funding acquisition, Methodology, Software, Investigation. **Luoyi Yan:** Methodology, Investigation. **Scott Whyte:** Funding acquisition, Methodology, Supervision, Writing – review & editing.

Declaration of Competing Interest

The authors declare the following financial interests/personal relationships which may be considered as potential competing interests: Zhiwei Gao reports financial support was provided by Royal Academy of Engineering.

Data availability

Data will be made available on request.

Acknowledgement

This research is funded by the Royal Academy of Engineering (UK) through the Industrial Fellowships (IF2122\149).

Appendix. The constitutive equations

The elastic relation stress–strain relationship is expressed as

$$de_{ij}^{e} = \frac{ds_{ij}}{2G} = \frac{pdr_{ij} + r_{ij}dp}{2G} \tag{19}$$

$$d\varepsilon_{v}^{e} = \frac{dp}{K} \tag{20}$$

where de_{ij}^{e} and $d\varepsilon_{v}^{e}$ denote the elastic deviatoric and volumetric strain increments, respectively. Since the total strain increment $d\varepsilon_{ij}$ is the summation of the elastic and plastic parts ($d\varepsilon_{ij} = d\varepsilon_{ij}^{e} + d\varepsilon_{ij}^{p}$), one can get the equation below based on the condition of consistency (Eq. (4)) and Eqs. (19) and (20)

$$2G\overline{n}_{ij}\left(de_{ij} - L\overline{n}_{ij}\right) - \overline{n}_{ij}r_{ij}K\left(d\varepsilon_{v} - \sqrt{2/3}\,LD\right) - K_{p}L = 0 \tag{21}$$

The loading index can then be determined from Eq. (21) as below

$$L = \Theta_{ij}d\varepsilon_{kl} \tag{22}$$

$$\Theta_{ij} = \frac{2G\overline{n}_{ij} - K\overline{n}_{pq}r_{pq}\delta_{ij}}{2G - \sqrt{2/3}KD\overline{n}_{ij}r_{ij} + K_{p}} \tag{23}$$

The relationship between stress and strain increments is expressed as

$$d\sigma_{ij} = E_{ijkl}d\varepsilon_{kl}^{e} = E_{ijkl}(d\varepsilon_{kl} - d\varepsilon_{kl}^{p}) = E_{ijkl}\left[d\varepsilon_{kl} - \left(de_{kl}^{p} + d\varepsilon_{v}^{p}\delta_{kl}/3\right)\right] \tag{24}$$

$$E_{ijkl} = (K - 2G/3)\delta_{ij}\delta_{kl} + G\left(\delta_{ki}\delta_{lj} + \delta_{li}\delta_{kj}\right) \tag{25}$$

The plastic strain increment can be obtained based on Eqs. (6)-(8)

$$d\varepsilon_{ij}^{p} = de_{ij}^{p} + d\varepsilon_{v}^{p}\delta_{ij}/3 = h(L)\left(\overline{n}_{ij} + \sqrt{2/27}\,D\delta_{ij}\right)\Theta_{kl}d\varepsilon_{kl} \tag{26}$$

Combining Eqs. (24) and (26), one can get

$$d\sigma_{ij} = E_{ijpq}\left[\delta_{pk}\delta_{ql} - h(L)\left(\overline{n}_{pq} + \sqrt{2/27}\,D\delta_{pq}\right)\Theta_{kl}\right]d\varepsilon_{kl} \tag{27}$$

The constitutive equations for the conventional step-by-step modelling. During the skipped-cycle modelling, the constitutive equations remain the same while two model parameters are scaled, one for the plastic modulus (h_m) and the other for the dilatancy relationship (d_1) as discussed before.

References

Abadie, C.N., Houlsby, G.T., Byrne, B.W., 2019. A method for calibration of the Hyperplastic Accelerated Ratcheting Model (HARM). Comput. Geotech. 112, 370–385.

Achmus, M., Kuo, Y.S., Abdel-Rahman, K., 2009. Behavior of monopile foundations under cyclic lateral load. Comput. Geotech. 36 (5), 725–735.

Andersen, K.H., 2009. Bearing capacity under cyclic loading - offshore, along the coast, and on land. the 21st bjerrum lecture presented in oslo. Can Geotech J. 46 (5), 513–535.

Andersen, K.H. 2005. Cyclic soil parameters for offshore foundation design. In: Meyer, editor, 3rd International Symposium on Frontiers in Offshore Geotechnics (ISFOG). Oslo, pp. 5–82.

Burd, H.J., Abadie, C.N., Byrne, B.W., Houlsby, G.T., Martin, C.M., McAdam, R.A., Jardine, R.J., Pedro, A.M.G., Potts, D.M., Taborda, D.M.G., Zdravković, L., Andrade, M.P., 2020. Application of the PISA design model to monopiles embedded in layered soils. Géotechnique 70 (11), 1067–1082.

Byrne, B.W., Houlsby, G.T., Burd, H.J., Gavin, K.G., Igoe, D.J.P., Jardine, R.J., Martin, C. M., McAdam, R.A., Potts, D.M., Taborda, D.M.G., Zdravković, L., 2020. PISA design model for monopiles for offshore wind turbines: application to a stiff glacial clay till. Géotechnique 70 (11), 1030–1047.

Corti, R., Diambra, A., Wood, D.M., Escribano, D.E., Nash, D.F., 2016. Memory surface hardening model for granular soils under repeated loading conditions. J Eng Mech. 142 (12), 04016102.

Duque, J., Ochmański, M., Mašín, D., Hong, Y., Wang, L., 2021. On the behaviour of monopiles subjected to multiple episodes of cyclic loading and reconsolidation in cohesive soils. Comput. Geotech 134, 104049.

François, S., Karg, C., Haegeman, W., Degrande, G., 2010. A numerical model for foundation settlements due to deformation accumulation in granular soils under repeated small amplitude dynamic loading. Int. J. Numer. Anal. Methods Geomech. 34 (3), 273–296.

Gao, Z., Zhao, J., 2015. Constitutive modelling of anisotropic sand behaviour in monotonic and cyclic loading. J Eng Mech. 141 (8), 04015017.

Gao, Z., Li, X., Lu, D., 2022. Nonlocal regularization of an anisotropic critical state model for sand. Acta Geotechnica. 17 (2), 427–439.

Gao, Z., Zhao, J., Li, X.S., Dafalias, Y.F., 2014. A critical state sand plasticity model accounting for fabric evolution. Int. J. Numer. Anal. Methods Geomech. 38 (4), 370–390.

Gourvenec, S., 2022. Whole Life Design: Theory and Applications of This New Approach to Offshore Geotechnics. Ind Geotech J 1–26.

Lai, Y., Wang, L., Hong, Y., Ben, H.e., 2020. Centrifuge modelling of the cyclic lateral behaviour of large-diameter monopiles in soft clay: Effects of episodic cycling and reconsolidation. Ocean Eng 200, 107048.

LeBlanc, C., Houlsby, G.T., Byrne, B.W., 2010. Response of stiff piles in sand to long-term cyclic lateral loading. Géotechnique 60 (2), 79–90.

Li, X.S., 2002. A sand model with state-dependent dilatancy. Géotechnique 52 (3), 173–186.

Li, X.S., Dafalias, Y.F., 2000. Dilatancy for cohesionless soils. Géotechnique 50 (4), 449–460.

Liao, D., Yang, Z., 2021. Hypoplastic modelling of anisotropic sand behaviour accounting for fabric evolution under monotonic and cyclic loading. Acta Geotech. 16, 2003–2029.

Liao, D., Yang, Z., Wang, S., Wu, W., 2022. Hypoplastic model with fabric change effect and semifluidized state for post-liquefaction cyclic behaviour of sand. Int. J. Numer. Anal. Methods Geomech. 1–24.

Ling, H.I., Yang, S., 2006. Unified sand model based on the critical state and generalized plasticity. J Eng Mech. 132 (12), 1380–1391.

Liu, H.Y., Kaynia, A.M., 2022. Monopile responses to monotonic and cyclic loading in undrained sand using 3D FE with SANISAND-MSu. Wat. Sci. Eng. 15 (1), 69–77.

Liu, H., Diambra, A., Abell, J.A., Pisanò, F., 2020. Memory-Enhanced plasticity modeling of sand behavior under undrained cyclic loading. J. Geotech. Geoenviron. Eng. 146 (11), 04020122.

Liu, H., Kementzetzidis, E., Abell, J.A., Pisanò, F., 2021. From cyclic sand ratcheting to tilt accumulation of offshore monopiles: 3D FE modelling using SANISAND-MS. Géotechnique 1–16.
Niemunis, A., Wichtmann, T., Triantafyllidis, T., 2005. A high-cycle accumulation model for sand. Comput. Geotech. 32 (4), 245–263.
Page, A.M., Klinkvort, R.T., Bayton, S., Zhang, Y., Jostad, H.P., 2021. A procedure for predicting the permanent rotation of monopiles in sand supporting offshore wind turbines. Mar. Struct. 75, 102813.
Pasten, C., Shin, H., Santamarina, J.C., 2014. Long-term foundation response to repetitive loading. J. Geotech. Geoenviron. Eng. 140 (4), 04013036.
Simonin, L.E., Houlsby, G. T., Byrne, B.W. 2003. HySand: A New Constitutive Model for Sand Under Cyclic Loading. In: International Conference of the International Association for Computer Methods and Advances in Geomechanics. 142-149. Springer, Cham.
Sloan, S.W., Abbo, A.J., Sheng, D., 2001. Refined explicit integration of elastoplastic models with automatic error control. Eng. Comput. 18 (1/2), 121–154.
Staubach, P., Wichtmann, T., 2020. Long-term deformations of monopile foundations for offshore wind turbines studied with a high-cycle accumulation model. Comput. Geotech. 124, 103553.
Suiker, A.S.J., de Borst, R., 2003. A numerical model for the cyclic deterioration of railway tracks. Int. J. Numer. Methods Eng. 57 (4), 441–470.
Taborda, D.M., Zdravković, et al., 2020. Finite-element modelling of laterally loaded piles in a dense marine sand at Dunkirk. Géotechnique 70 (11), 1014–1029.
Truong, P., Lehane, B.M., Zania, V., Klinkvort, R.T., 2019. Empirical approach based on centrifuge testing for cyclic deformations of laterally loaded piles in sand. Géotechnique. 69 (2), 133–145.
Wang, G., Xie, Y., 2014. Modified bounding surface hypoplasticity model for sands under cyclic loading. J. Eng. Mech. 140 (1), 91–101.
Wang, Z.L., Dafalias, Y.F., Shen, C.K., 1990. Bounding surface hypoplasticity model for sand. J. Eng. Mech. 116 (5), 983–1001.
Whyte, S.A., Burd, H.J., Martin, C.M., Rattley, M.J., 2020. Formulation and implementation of a practical multi-surface soil plasticity model. Comput. Geotech. 117, 103092.
Wichtmann, T., 2005. Explicit accumulation model for non-cohesive soils under cyclic loading. Ruhr Univ, Bochum, Bochum, Germany. Ph.D. thesis.
Wichtmann, T., Niemunis, A., Triantafyllidis, T., 2010. Strain accumulation in sand due to drained cyclic loading: on the effect of monotonic and cyclic preloading (Miner's rule). Soil Dyn. Earthq. Eng. 30 (8), 736–745.
Yang, M., Taiebat, M., Dafalias, Y.F., 2002. SANISAND-MSf: a sand plasticity model with memory surface and semifluidised state. Géotechnique 72 (3), 227–246.
Yang, Z., Elgamal, A., Parra, E., 2003. Computational model for cyclic mobility and associated shear deformation. J Geotech Geoenviron. 129 (12), 1119–1127.
Yin, Z., Jin, Y., Shen, J., Huang, H., 2017. An efficient optimization method for identifying parameters of soft structured clay by an enhanced genetic algorithm and elastic-viscoplastic model. Acta Geotech. 12 (4), 849–867.
Yin, Z., Jin, Y., Shen, J., Hicher, P.Y., 2018. Optimization techniques for identifying soil parameters in geotechnical engineering: Comparative study and enhancement. Int. J. Numer. Anal. Methods Geomech. 42 (1), 70–94.
Zachert, H., Wichtmann, T., Triantafyllidis, T., Hartwig, U. Simulation of a full-scale test on a gravity base foundation for offshore wind turbines using a high cycle accumulation model. In 3rd International Symposium on Frontiers in Offshore Geotechnics (ISFOG), Oslo.2015.